Hybrid equation of state approach in binary neutron-star merger simulations

A. Figura,[1,3] Jia-Jing Lu (陆家靖),[2] G. F. Burgio,[1] Zeng-Hua Li (李增花),[2] and H.-J. Schulze[1]

[1]*INFN Sezione di Catania, Dipartimento di Fisica, Universitá di Catania,*
Via Santa Sofia 64, 95123 Catania, Italy
[2]*Institute of Modern Physics, Key Laboratory of Nuclear Physics and Ion-beam Application (MOE),*
Fudan University, Shanghai 200433, People's Republic of China
[3]*Institut für Theoretische Physik, Universität Frankfurt, Max von Laue Strasse 1,*
60438 Frankfurt, Germany

We investigate the use of hybrid equations of state in binary neutron-star simulations in full general relativity, where thermal effects are included in an approximate way through the adiabatic index Γ_{th}. We employ a newly developed finite-temperature equation of state derived in the Brueckner-Hartree-Fock approach and carry out comparisons with the corresponding hybrid versions of the same equation of state, investigating how different choices of Γ_{th} affect the gravitational-wave signal and the hydrodynamical properties of the remnant. We also perform comparisons with the widely used Steiner-Fischer-Hempel equation of state, detailing the differences between the two cases. Overall, we determine that when using a hybrid equation of state in binary neutron-star simulations, the value of the thermal adiabatic index $\Gamma_{th} \approx 1.7$ best approximates the dynamical and thermodynamical behavior of matter computed using complete, finite-temperature equations of state.

I. INTRODUCTION

The numerical simulation of neutron-star (NS) mergers requires as a most essential input the equation of state (EOS) of the stellar matter under the relevant conditions of particle composition, partial densities, and temperature.

Comparing and contrasting the results of simulations and the observed gravitational-wave signal, then allows us to constrain theoretical models for the EOS and extract quantitatively the essential features of the EOS. The availability of such data has already permitted this selection process and, in the future, rapid progress is to be expected toward the identification of "the" EOS of dense nuclear matter [1,2].

Theoretical EOSs have been computed in various approaches, in particular for cold nuclear matter, but much less for hot matter up to the temperatures (about 50 MeV) occurring during the merger. In this article we propose and analyze a finite-temperature EOS derived within the Brueckner-Hartree-Fock (BHF) many-body approach that has already been shown to satisfy all current experimental and observational constraints on nuclear matter [3], in particular those imposed by the merger event GW170817 [4,5].

We perform here the first binary NS merger simulations with this EOS and investigate, in particular, the effects of different approximations for the treatment of finite temperature in the simulations, following Ref. [6]. The motivation is to understand how much the widely used "hybrid-EOS" approach impacts the gravitational-wave properties in binary

NS mergers; indeed, since this approach remains the only viable choice when using a zero-temperature EOS, it is important to examine which differences are to be expected with respect to simulations where finite-temperature versions of the same EOS are employed. In this context, the understanding of the best setup to be used in the approximate description is of great importance and can be carried out only by considering the full temperature-dependent EOS. In particular, we have carried out a number of simulations of merging NSs in full general relativity, employing two fully tabulated, temperature-dependent EOSs and a neutrino-leakage scheme for the treatment of neutrinos. At the same time, we have performed similar simulations employing hybrid EOSs whose cold part is represented by the slice at $T = 0$ of the temperature-dependent EOSs and where we have considered a variety of values for the thermal adiabatic index Γ_{th}. In this way, and summarizing the results of a number of simulations, we conclude that the value of $\Gamma_{th} \approx 1.7$ best approximates the complete, finite-temperature EOS in binary NS simulations.

The article is organized as follows. We first review in Sec. II the computation of the EOS in the BHF formalism, with different approximations for the finite-temperature part. Our numerical setup and methods are introduced in Sec. III. Results of the simulations are presented in Sec. IV, and conclusions are drawn in Sec. V. Technical details regarding the evaluation of gravitational-wave signal properties are given in the Appendix.

II. EQUATION OF STATE AT FINITE TEMPERATURE

A. The microscopic BHF approach: The V18 EOS

We only provide here a brief overview of the formalism, and refer to the various indicated references for full details, while a more detailed analysis can be found in [7]. We here compute the EOS in the BHF approach for asymmetric nuclear matter at finite temperature [8–16]. The essential ingredient of this approach is the interaction matrix K, which satisfies the following equations

$$K(n_B, x_p; E) = V + V \, \text{Re} \sum_{1,2} \frac{|12\rangle(1 - n_1)(1 - n_2)\langle 12|}{E - e_1 - e_2 + i0} K(n_B, x_p; E) \tag{1}$$

and

$$U_1(n_B, x_p) = \text{Re} \sum_2 n_2 \langle 12|K(n_B, x_p; e_1 + e_2)|12\rangle_a, \tag{2}$$

where $n(k)$ is a Fermi distribution, $x_p \equiv n_p/n_B$ is the proton fraction, and n_p and n_B are the proton and the total baryon number densities, respectively. (In the following, we will also use the notation $\rho_i \equiv m_N n_i$ and $\rho \equiv m_N n_B$ for the rest-mass densities, where $m_N = 1.67 \times 10^{-24}$ g is the nucleon mass). Here, E is the starting energy and $e(k) \equiv k^2/2m + U(k)$ is the single-particle energy. The multi-indices 1,2 denote in general momentum, isospin, and spin. In the present calculations, we adopt the Argonne V_{18} [17] potential as a realistic nucleon-nucleon interaction V supplemented with compatible microscopic three-nucleon forces derived by employing the same meson-exchange parameters as the two-body potential [18–21].

Regarding the extension to finite temperature, we use the so-called frozen-correlations approximation [9–12,16], and approximate the single-particle potentials $U_{n,p}(k)$ by the ones calculated at $T = 0$. Within this approximation, the nucleonic free energy density has the following simplified expression,

$$f_N = \sum_{i=n,p} \left[2 \sum_k n_i(k) \left(\frac{k^2}{2m_i} + \frac{1}{2} U_i(k) \right) - T s_i \right], \tag{3}$$

where

$$s_i = -2 \sum_k (n_i(k) \ln n_i(k) + [1 - n_i(k)] \ln [1 - n_i(k)]) \tag{4}$$

is the entropy density for the component i treated as a free Fermi gas with spectrum $e_i(k)$. From the total free energy density $f = f_N + f_L$ including lepton contributions, all relevant observables can be computed in a thermodynamically consistent way; namely one defines the chemical potentials

$$\mu_i = \frac{\partial f}{\partial n_i}, \tag{5}$$

which allow one to calculate the composition of betastable stellar matter, and then the total pressure p and the specific internal energy ε,

$$p = n_B^2 \frac{\partial (f/n_B)}{\partial n_B} = \sum_i \mu_i n_i - f, \tag{6}$$

$$\varepsilon = \frac{f + Ts}{\rho}, \qquad s = -\frac{\partial f}{\partial T}, \tag{7}$$

so that $e \equiv \rho(1 + \varepsilon)$ is the total energy density.

In practice, numerical parametrizations for the free energy density of symmetric nuclear matter (SNM) and pure neutron matter (PNM) were given in Ref. [7], and for asymmetric nuclear matter a parabolic approximation for the x_p dependence is used [13,22–24],

$$f(n_B, T, x_p) \approx f_{\text{SNM}}(n_B, T) + (1 - 2x_p)^2 [f_{\text{PNM}}(n_B, T) - f_{\text{SNM}}(n_B, T)]. \tag{8}$$

This specifies the V18 EOS for arbitrary values of baryon density, proton fraction, and temperature, which can then be employed in merger simulations, or simply for computing the mass-radius relation of cold and hot NSs by solving the Tolmann-Oppenheimer-Volkov (TOV) equations for charge-neutral betastable matter including leptons. We also report that the V18 EOS becomes acausal at $n_B = 0.75$ fm^{-3} ($\rho \approx 1.3 \times 10^{15}$ g/cm^3; see, e.g., Ref. [25]); this density, however, is far from ever being reached in the simulations (see Fig. 4 and related discussion).

Since our EOS accounts only for homogeneous matter in the core region of the NS, we properly extend the EOS, for every temperature and proton fraction, with an EOS for the crust, which we define as that covering the range in rest-mass densities $\rho \lesssim 10^{14}$ g/cm^3. In particular, we choose the Shen EOS [26] for that purpose. Furthermore, an artificial low-density background atmosphere, $\rho \lesssim 10^3$ g/cm^3, evolved as discussed in [27], is used in all our simulations.

B. The phenomenological SFHo EOS

As an alternative to the temperature-dependent V18 EOS and to extend and strengthen the results of our comparison we have also considered the phenomenological Steiner-Fischer-Hempel (SFHo) EOS [28,29]. We recall that phenomenological approaches are commonly used in simulations of core-collapse supernovae and NS mergers, where a wide range of densities, temperatures, and charge fractions describing both clustered and homogeneous matter has to be covered. Some of the most commonly used finite-temperature EOSs are the ones by Lattimer and Swesty [30] and Shen *et al.* [31]. In both cases, matter is modeled as a mixture of heavy nuclei treated in the single-nucleus approximation, α particles, and free neutrons and protons immersed in a uniform gas of leptons and photons. In the former case, nuclei are described within the liquid-drop model, and a simplified Skyrme interaction is used for nucleons; in the latter case a relativistic mean field (RMF) model based on the TM1 interaction [32] is used for nucleons. In both approaches, all light nuclei are ignored, except for alpha particles. This drawback has been overcome in the SFHo EOS model of Hempel and Schaffner-Bielich (HS) [28] and Hempel *et al.* [29], which goes beyond the single-nucleus approximation, and takes into account a statistical ensemble of nuclei and interacting nucleons. Nuclei are described as classical Maxwell-Boltzmann particles, and nucleons are treated within the RMF model employing different parametrizations.

Here, we adopt the new SFHo EOS [33], which is based on the HS EOS but implemented with a new RMF parametrization fitted to some NS radius determinations. The new RMF parameters are varied to ensure that saturation properties of nuclear matter are correctly reproduced. In particular, the nuclear incompressibility $K = 245$ MeV turns out to be compatible with the currently acceptable range of 240 ± 20 MeV [34], which agrees with that predicted from the giant monopole resonances. Moreover, the new parametrization ensures that the symmetry energy at saturation density $J = 32.8$ MeV is well within the empirical range 28.5–34.9 MeV [35], and that the NS maximum mass $M_{\mathrm{TOV}} = 2.06\ M_\odot$ is (marginally) compatible with the currently strongest observational constraint $M > 2.14^{+0.10}_{-0.09}\ M_\odot$ [36].

As an illustration of the properties of the two temperature-dependent EOSs, Fig. 1 shows the pressure p and energy density e of betastable matter as a function of the baryon number density for both the V18 and SFHo EOSs. In particular, in the left panel we display the energy density (solid curves) and pressure (dashed curves) as a function of the baryon density obtained at $T = 0$ for the V18 case and the SFHo EOS. We notice that the V18 EOS is stiffer than SFHo and this will play an important role in the discussion and interpretation of the simulation results. In the right panel, on the other hand, we display the thermal contributions to the betastable EOS defined as

$$p_{\mathrm{th}}(\rho, T) \equiv p(\rho, T) - p(\rho, 0), \tag{9}$$

$$e_{\mathrm{th}}(\rho, T) \equiv \rho[\varepsilon(\rho, T) - \varepsilon(\rho, 0)], \tag{10}$$
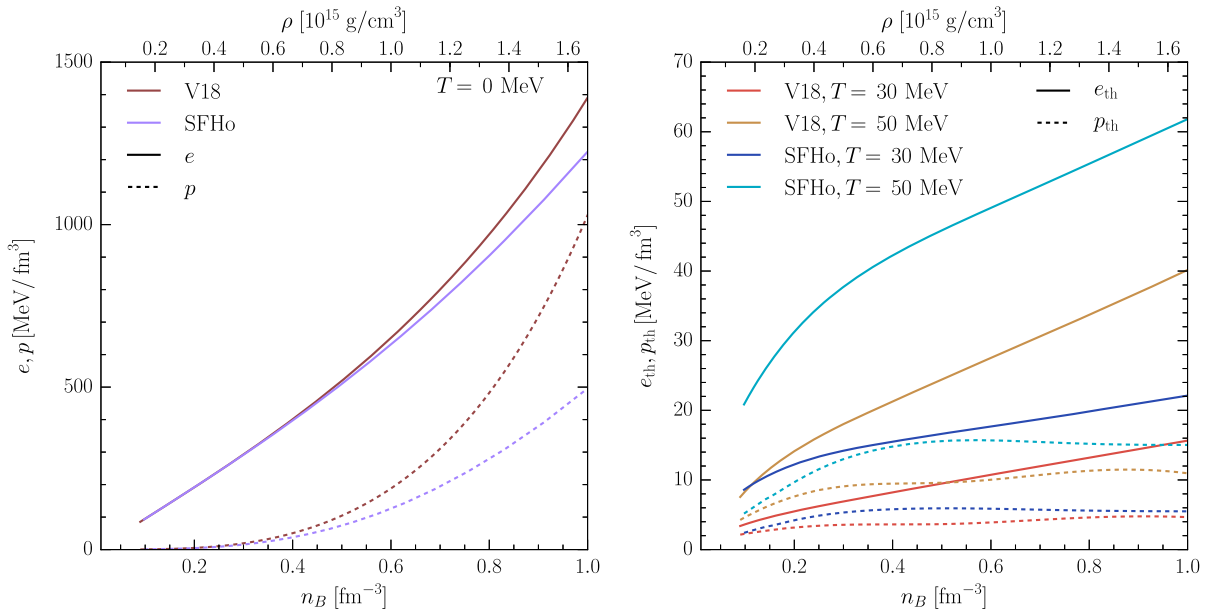

FIG. 1.   Left panel: pressure p and energy density e of betastable matter at $T = 0$ as a function of the baryon number density. Right panel: thermal pressure and internal energy density, Eqs. (9), (10) at different temperatures. Results with V18 and SFHo EOSs are compared.

for different temperatures ($T = 30, 50$ MeV) and where e_{th} is the internal energy density. One can notice that in the V18 case the overall thermal effects are smaller than in SFHo, of the order of a few percent at high density, even at the fairly high temperature $T = 50$ MeV considered here (see [37] for a study on uncertainties of finite-temperature properties of neutron matter). In Ref. [7] we examined in detail for the V18 case the intricate interplay between the nucleonic and leptonic contributions to the betastable EOS, which are of equal importance.

C. Hybrid-EOS approach

An approach often employed in simulations of NS mergers [6,38–52] is the so-called "hybrid EOS," in which pressure and the specific internal energy can be expressed as the sum of a "cold" contribution obeying a zero-temperature EOS, and of a "thermal" contribution obeying the ideal-fluid EOS (see [53] for details). In this approach, the relation between the thermal pressure and the internal energy density of betastable matter can be expressed as

$$p_{th}(\rho, T) = e_{th}(\Gamma_{th} - 1), \tag{11}$$

where Γ_{th} is the thermal adiabatic index appearing in the ideal-fluid approximation. In a temperature-dependent approach, this quantity becomes dependent on density and temperature, i.e., $\Gamma_{th} \equiv 1 + p_{th}/e_{th}$, and this dependence is illustrated in Fig. 2 with dashed curves for the V18 (left panel) and for the SFHo EOS (right panel). Note that there is a clear density dependence, whereas the temperature dependence turns out to be less pronounced. Overall,

the thermal adiabatic index remains above 1.5 at all densities in the SFHo case, but decreases below 1.5 in the V18 case, consistent with the thermal pressures shown in Fig. 1.

In temperature-dependent EOSs to be used in numerical simulations, the adiabatic index is usually not defined for betastable matter (featuring different proton fractions in hot and cold matter), but can be computed at constant proton fraction as

$$\Gamma_{th}(\rho, T) \equiv 1 + \frac{p(\rho, x_\beta, T) - p(\rho, x_\beta, 0)}{\rho[\varepsilon(\rho, x_\beta, T) - \varepsilon(\rho, x_\beta, 0)]}, \tag{12}$$

where x_β is the betastable proton fraction at either $(\rho, T > 0)$ or $(\rho, T = 0)$. This leads to different numerical values that are also displayed in Fig. 2, where the solid (dash-dotted) curves display results with x_β taken at $T > 0$ ($T = 0$) for the V18 (left panel) and the SFHo EOS (right panel), respectively. We note that this procedure yields values $1.5 \lesssim \Gamma_{th} \lesssim 1.7$ for the V18 EOS, and $1.6 \lesssim \Gamma_{th} \lesssim 1.8$ for the SFHo EOS, whereas the average value for the betastable matter is smaller in both cases. We point out, however, that in the merger simulations the matter in the early remnant is usually not in beta equilibrium and therefore all the values shown in Fig. 2 can only give qualitative indications of effective Γ_{th} values. This will be discussed in more detail later.

In fact, three-dimensional hydrodynamical calculations of NS mergers in the conformally flat approximation of general relativity reported in Ref. [6] have questioned the validity of a constant-Γ_{th} approximation in the hybrid-EOS
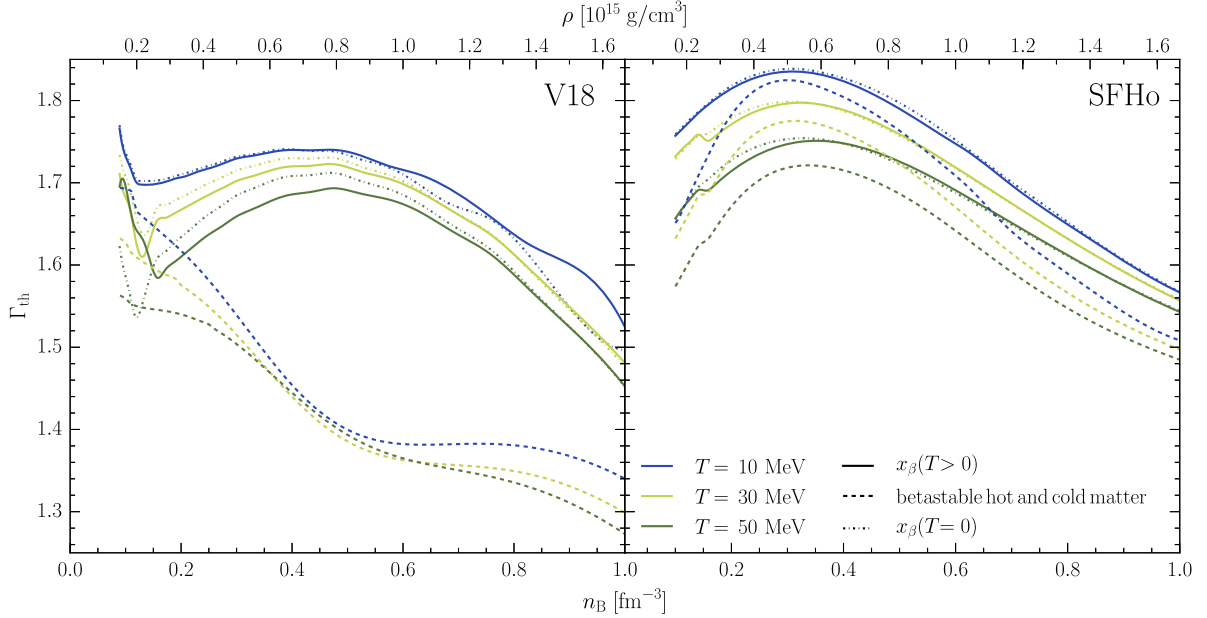

FIG. 2.   Adiabatic index of betastable matter, Eq. (12), as a function of density at different temperatures. Dashed curves show results obtained from betastable hot and cold matter, while for the solid (dash-dotted) curves the proton fraction is fixed to the one of betastable hot (cold) matter (see discussion in the text).
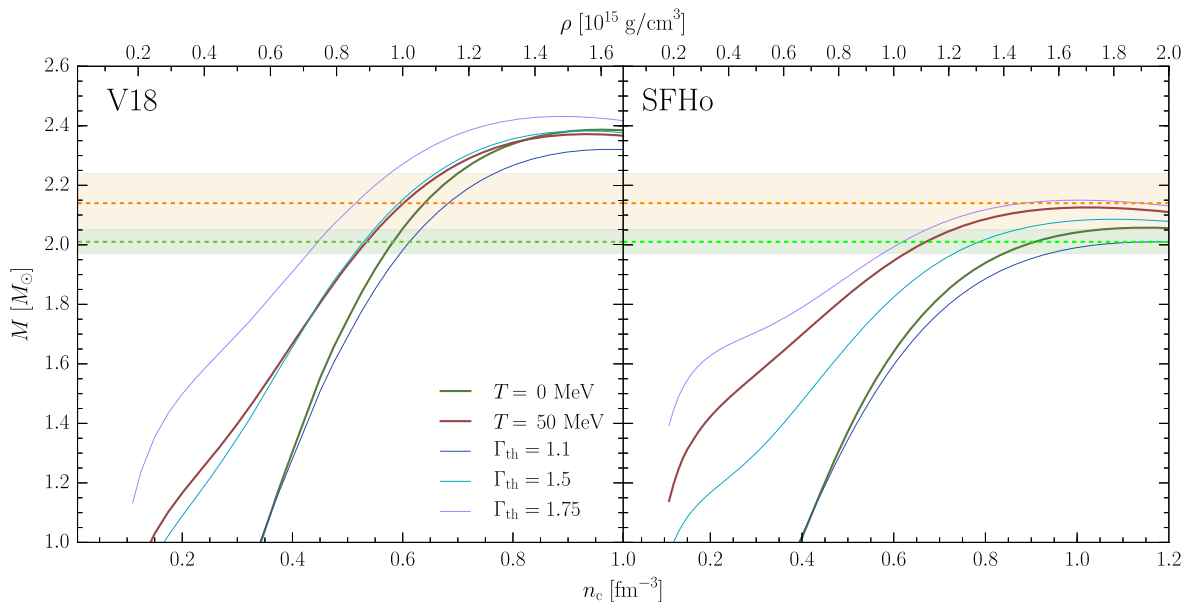
FIG. 3. Gravitational mass as a function of the central rest-mass density for $T = 0$ and $T = 50$ MeV with full temperature treatment, and different choices of constant $\Gamma_{\mathrm{th}} = 1.1, 1.5, 1.75$ at $T = 50$ MeV. Dashed orange and green lines, together with the shaded regions of the same color, refer to the observational constraints of Refs. [36,61], respectively.

approach (originally chosen as $\Gamma_{\mathrm{th}} \approx 1.5$ [38]), especially in the postmerger phase, where thermal effects are most relevant. Strong variations were found in both the oscillation frequency of the forming hypermassive NS (HMNS), and the delay time between the merger and black-hole formation, with respect to the simulations with a fully consistent treatment of the temperature. It is one of our goals here to reconsider—by comparing and contrasting fully general-relativistic simulations with temperature-dependent and hybrid EOSs—the issue of the most appropriate constant value of Γ_{th} to be employed when adding a thermal component to the EOS.

D. Macroscopical properties of the V18 and SFHo EOSs

Given the widespread recent use of hybrid EOSs [41–52,54–56] and the scarcity of fully temperature-dependent EOSs (that are effectively restricted to a handful 60–29,33,57]]), the determination of the most realistic value to be used for Γ_{th} is not purely academic. Indeed, even at the lowest-order approximation, Γ_{th} has an impact on the stability of the merger remnant and hence of its lifetime before collapsing to a black hole. This is most easily shown in Fig. 3, which reports sequences of non-rotating equilibrium models as a function of the central rest-mass density (or baryon number density) for the V18 EOS (left panel) and the SFHo EOS (right panel). Different curves refer to different temperatures (i.e., $T = 0$ and $T = 50$ MeV), using the exact temperature dependence and three different choices of constant $\Gamma_{\mathrm{th}} = 1.1, 1.5, 1.75$. In other words, we use Eq. (10) at $T = 50$ MeV and the

estimate of the thermal adiabatic index to compute the thermal contribution to the pressure, Eq. (11).[1]

Note the weak dependence of the maximum TOV mass on the temperature, so that for the V18 EOS we have that $M_{\mathrm{TOV}}(T = 0) \equiv M_{\mathrm{TOV}} = 2.387 \, M_\odot$ at a central rest-mass density $\rho_c = 1.58 \times 10^{15} \, \mathrm{g/cm^3}$ (corresponding to a baryon number density $n_c = 0.96 \, \mathrm{fm^{-3}}$), while $M_{\mathrm{TOV}}(T = 50 \, \mathrm{MeV}) = 2.372 \, M_\odot$ at $\rho_c = 1.53 \times 10^{15} \, \mathrm{g/cm^3}$ $(n_c = 0.93 \, \mathrm{fm^{-3}})$. This is mainly due to the competition of three different effects for fixed density and increasing temperature, namely (a) the increase of the thermal pressures of neutrons and protons, (b) the increase of the isospin symmetry due to betastability, which reduces the baryonic pressure, and (c) the increase of the lepton thermal pressure. In particular, the V18 EOS is characterized by large values of the symmetry energy which increases with temperature and density, and this is due to the strongly repulsive character of the microscopic three-body forces. This implies a strong increase of the isospin symmetry with temperature and density [7].

In Fig. 3, left panel, the $\Gamma_{\mathrm{th}} = 1.5$ approximation at $T = 50$ MeV happens to yield a very similar result as the full calculation; hence we can conclude that for the V18 EOS, the value of the adiabatic thermal index $\Gamma_{\mathrm{th}} = 1.5$ represents the best approximation for betastable matter at finite temperature as it is the one that best mimics the effects of a full temperature dependence. The proton fraction x_p corresponding to betastability is quite different at $T = 0$

---

[1]For this plot, a cold crust is attached to the isothermal NS interior at $n_B = 0.08 \, \mathrm{fm^{-3}}$, corresponding to $\rho \approx 1.32 \times 10^{14} \, \mathrm{g/cm^3}$.

and finite T at given baryon density, and therefore the Γ_{th} computed in this way is different from the one calculated at the same x_p in both cold and hot matter, using either the x_p of cold matter or the one of hot matter in Eq. (12). The latter is the choice made in the numerical simulations and, according to Fig. 2, typical values of $\Gamma_{th} \sim 1.7$ in this choice correspond to typical values of $\Gamma_{th} \sim 1.5$ in the betastable procedure, which is the one used in Fig. 3.

On the other hand, $\Gamma_{th} = 1.1$ and 1.75 predict lower and higher M_{TOV}, respectively, according to the lower and higher thermal pressure they provide. One can appreciate the opposite effects of p_{th} and e_{th} on the maximum mass: When including only e_{th} ($\Gamma_{th} = 1.1$ curves featuring very small p_{th}), M_{TOV} decreases with respect to the cold $M_{TOV}(T = 0)$, whereas including also p_{th} [fully tabulated (FT), $\Gamma_{th} = 1.5, 1.75$ curves] M_{TOV} increases again. For the V18 FT EOS there is nearly compensation between both effects due to a relatively low thermal pressure induced by a strong change of the proton fraction in hot vs cold matter, and the related changes of hadronic and leptonic contributions to the pressure that compete with each other, as explained before.

The right panel of Fig. 3 reports the corresponding results for the SFHo case, and in this case we can note a larger temperature dependence of the maximum TOV mass when compared to the V18 case; in turn, this relates to the higher thermal pressure and adiabatic index for the SFHo. This is due to the smaller change of the proton fraction with increasing temperature, which causes a larger thermal pressure, at variance with the V18-EOS case. Consequently, the full calculation at $T = 50$ MeV seems to be better reproduced by the $\Gamma_{th} \simeq 1.7$ approximation here.

The maximum masses are then $M_{TOV}(T = 0) \equiv M_{TOV} = 2.058\ M_\odot$, with a central rest-mass density $\rho_c = 1.90 \times 10^{15}$ g/cm^3 ($n_c = 1.15$ fm^{-3}), and $M_{TOV}(T = 50$ MeV$) = 2.126\ M_\odot$, with $\rho_c = 1.68 \times 10^{15}$ g/cm^3 ($n_c = 1.02$ fm^{-3}). These values, together with other useful information such as the rotation frequencies at the mass-shedding limit, are summarized in Table I.

TABLE I. Properties of the maximum-mass configurations of both static and maximally rotating stars with Kepler frequency at temperatures $T = 0$ and 50 MeV: gravitational and baryonic masses M and M_B, and the equatorial radius R.

EOS	f (Hz)	T (MeV)	$M\ (M_\odot)$	$M_B\ (M_\odot)$	R (km)
V18	0	0	2.387	2.913	10.86
	0	50	2.372	2.785	11.40
	1770	0	2.845	3.385	14.17
	1590	50	2.724	3.102	15.00
SFHo	0	0	2.058	2.448	10.30
	0	50	2.126	2.450	11.81
	1741	0	2.472	2.911	13.73
	1376	50	2.413	2.726	15.98

Finally, we note that the merger remnant is expected to be rotating differentially and to support a mass which is upper bounded by the threshold mass to prompt collapse to a black hole, that can be estimated to be [62]

$$M_{th} = M_{TOV}\left(3.06 - \frac{1.01}{1 - 1.34 M_{TOV}/R_{TOV}}\right). \quad (13)$$

For the V18 EOS, the threshold mass amounts to $M_{th} = 3.04\ M_\odot$ with $M_{TOV}/R_{TOV} = 0.324$, whereas in the SFHo case $M_{th} = 2.86\ M_\odot$, being $M_{TOV}/R_{TOV} = 0.295$ (in geometrized units with $c = 1 = G = M_\odot$).

III. INITIAL DATA AND NUMERICAL PROCEDURE OF MERGER SIMULATIONS

The mathematical and numerical setup considered here is similar to the one discussed in great detail in Ref. [63]; we review here only the main aspects and differences with respect to this reference, referring the interested reader to the latter for additional information. We consider initial data for irrotational binary neutron stars computed using the multidomain spectral-method code LORENE [64,65]. All initial data have been modeled considering a zero-temperature, beta-equilibrated cut of the full EOS table (which will be labeled from now on as "cold EOS"), and involve, in our case, equal-masses binaries with a gravitational mass $M = 1.35\ M_\odot$ at infinite separation (corresponding to a total baryonic mass $M_B = 2.97\ M_\odot$ with the V18 EOS and $M_B = 2.96\ M_\odot$ with the SFHo EOS, as Table I), and an initial separation between the stellar centers of 45 km.

We then proceed to study two different implementations of our finite-temperature EOS:

(a) The FT case, in which a local temperature is obtained by inverting the $e(\rho, x_p, T)$ entries in the EOS table, using the values of the internal energy density e, rest-mass density ρ, and proton fraction x_p obtained through the solution of the hydrodynamics equations at a given time step. This temperature is then used to obtain the total pressure $p(\rho, x_p, T)$ from the same EOS table.

(b) The "hybrid-EOS" method discussed in Sec. II C, where finite-temperature effects caused in particular by shock heating during the postmerger phase are taken into account by enhancing the zero-temperature EOS with an ideal-fluid contribution [38,53]. In this method, the local pressure is approximated by

$$p = p_c + \rho(\varepsilon - \varepsilon_c)(\Gamma_{th} - 1), \quad (14)$$

using the values $\varepsilon_c(\rho)$ and $p_c(\rho)$ of the cold EOS table for *betastable* matter and the local propagated values of ρ and ε. In this case no local temperature (and no proton fraction) can be extracted during the simulation. The adiabatic index Γ_{th} is a constant both in space and time, constrained mathematically and from first principles to be $1 \leq \Gamma_{th} \leq 2$ [66]. However, in order to properly compare a simulation of

type (b) with the corresponding simulation of type (a), the cold part of the hybrid EOS is chosen to match the $T = 0$ slice of the temperature-dependent EOS. In this way, the solutions of type (a) and (b) are identical during the inspiral —when shocks are absent or minute and confined to the stellar surfaces—but start to differ after the merger, when thermal effects develop. Clearly, we consider the simulations of type (a) as the most realistic ones and iterate the values of Γ_{th} in simulations of type (b) to find the closest match in the bulk behavior of the matter.

Overall, for our V18 EOS we consider five different binary merger simulations, namely the reference FT case [i.e., one simulation of type (a)] and four additional simulations in which the value of Γ_{th} is varied [i.e., four simulations of type (b)]. In particular, we consider the limiting case of $\Gamma_{th} = 1.1$, representative of the cold case with almost absent thermal effects: the case $\Gamma_{th} = 1.5$, which best approximates the V18 EOS in the betastable regime at $T = 50$ MeV according to Figs. 2 and 3, the case $\Gamma_{th} = 1.7$, which best approximates the FT results in the simulations, and, finally, the case $\Gamma_{th} = 1.75$ with the largest thermal contributions, which also represents a common choice in the literature (see Refs. [6,55] for discussions on the use of different Γ_{th}). In addition, we also perform three more simulations with the SFHo EOS, one in the FT regime and two using the hybrid-EOS approach with $\Gamma_{th} = 1.5$ and $\Gamma_{th} = 1.75$.

All simulations are performed in full General Relativity using the fourth-order finite-differencing code of McLachlan [67], which is part of the publicly available Einstein Toolkit [68]. The code solves the CCZ4 formulation of the Einstein equations [69–71], with a "1+log" slicing condition and a "Gamma driver" shift condition (see, e.g., Refs. [72,73]). The general-relativistic hydrodynamics equations are solved using the WhiskyTHC code [27,74,75], which uses either finite-volume or high-order finite-differencing high-resolution shock-capturing methods. We employ, in particular, the local Lax-Friedrichs Riemann solver and the high-order MP5 primitive reconstruction [76,77]. For the time integration of the coupled set of hydrodynamic and Einstein equations we use the method of lines with an explicit third-order Runge-Kutta method, with a Courant-Friedrichs-Lewy number of 0.15 to compute the time step.

Although matter compression and shocks increase the temperature of the remnant to several tens of MeV [78], neutrino emission acts as a cooling mechanism and is implemented in the temperature-dependent simulations, as only in the latter the electron fraction is consistently evolved in time. In these cases, we treat the effects on matter due to weak reactions using the gray (energy-averaged) neutrino-leakage scheme described in Refs. [79,80], and evolve free-streaming neutrinos according to the M0 heating scheme introduced in Refs. [48,80].

To ensure the nonlinear stability of the spacetime evolution, we add a fifth-order Kreiss-Oliger-type artificial dissipation [81]. We employ an adaptive-mesh-refinement

approach, where the grid hierarchy is handled by the Carpet driver [82]. Such a hierarchy consists of six refinement levels with a grid resolution varying from $h_5 = 0.16\ M_\odot$ (i.e., ~236 m) for the finest level, corresponding to about 40 points covering the NS radius on the equatorial plane at the beginning of the simulation for both the V18 and SFHo models, to $h_0 = 5.12\ M_\odot$ (i.e., ~7.5 km) for the coarsest level, whose outer boundary is at $1024\ M_\odot$ (i.e., ~1515 km). To reduce computational costs, we adopt a reflection symmetry across the $z = 0$ plane. While the V18 simulations presented here follow the remnant evolution for a timescale of at least 20 ms, the SFHo simulations are stopped a few milliseconds after the collapse to a black hole.

Before concluding this section, a couple of remarks are useful. First, the hybrid-EOS simulations are carried out using the betastable tables at $T = 0$, so that the simulation is "forced" to treat betastable matter corrected with the already-described finite-temperature effects. The FT simulation, on the other hand, is free to drive away from the betastable condition, and indeed this is what happens starting from the very beginning, as we will discuss in the next section. Second, the simulations employing the V18 EOS discussed here represent the first application of such recently derived and publicly available temperature-dependent EOS [83].

IV. NUMERICAL RESULTS

In the following we present the results of our binary NS merger simulations. Technical details regarding the extraction of the gravitational-wave signal are given in the Appendix.

A. Bulk dynamics

Following the considerations made in Sec. II for the V18 EOS and the chosen total binary mass $2.7\ M_\odot$, the merger simulations do not feature an immediate collapse to a black hole, but produce a metastable HMNS up to the largest time $t \approx 20$ ms that we reached in the simulations. At that time, the remnant is still stabilized by differential rotation and finite-temperature contributions to the pressure. This feature seems to be compatible with the multimessenger analysis of the GW170817 event [84]. On the other hand, the simulations performed with the SFHo EOS lead to a rather rapid collapse into a black hole, which seems to be in contrast with the expected amount of mass ejected in the GW170817 event.

Figure 4 shows in the two top panels the evolution of the maximum rest-mass density, ρ_{max}, for the different cases we have studied, while the third and fourth panels report the evolution of both the maximum and the density-weighted-average temperature

$$\langle T \rangle \equiv \frac{\int dV \rho T}{\int dV \rho}, \tag{15}$$

where the average is performed on the $z = 0$ plane, after applying a low-density threshold of 10^{13} g/cm³ to avoid
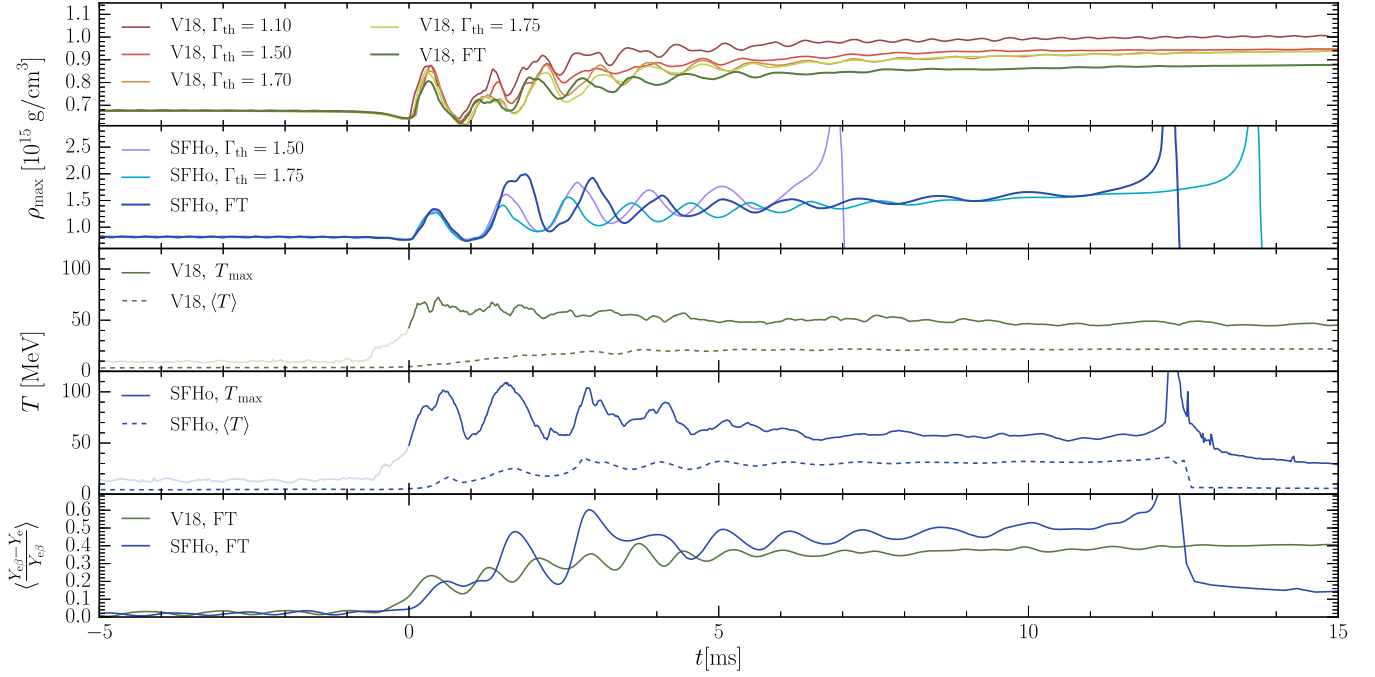
FIG. 4.   Maximum values of rest-mass density (upper panels) and temperature (third and fourth panels from the top, only for the simulations using the FT EOSs) as a function of time. The evolution of the average temperature $\langle T \rangle$, Eq. (15), is also displayed. A lighter color is chosen for the inspiral phase, where such temperatures are meant as representative only and do not reflect an accurate description of the thermodynamics of the matter. The average deviation from betastability, Eq. (16), is also represented in the lowest panel for both FT EOSs.

contamination from the very light but very hot matter ejected; only for the SFHo case, we change this threshold to 10^{10} g/cm^3 in order to also calculate the averaged quantities even after the collapse. A lighter color is chosen for the inspiral phase, where such temperatures are meant as representative only and do not reflect an accurate description of the thermodynamics of the matter. A similar behavior (and even larger inspiral temperatures) has been found also for other temperature-dependent EOSs, e.g., Refs. [85–87]. In the lowest panel we also show for both FT EOSs the density-weighted-average relative deviation from beta stability

$$\left\langle \frac{\Delta Y_{e\beta}}{Y_e} \right\rangle \equiv \frac{\int dV \rho \frac{|Y_{e\beta} - Y_e|}{Y_{e\beta}}}{\int dV \rho}, \qquad (16)$$

where $Y_{e\beta}(\rho, T)$ represents the electron fraction calculated pointwise on the $z = 0$ plane assuming beta equilibrium at the local density ρ and temperature T. For the V18 EOS it stabilizes at a fairly large reduction of about 40%, which will be discussed later in more detail. We set our time coordinate such that $t = t_{\text{merg}} = 0$, where t_{merg} is the time of the merger and corresponds to the maximum of the gravitational-wave amplitude, for all the cases we study.

When considering V18-EOS simulations, we find that, unsurprisingly, the $\Gamma_{\text{th}} = 1.1$ simulation produces the remnant with the highest maximum rest-mass density

$(\rho_{\text{max}} \approx 10^{15}$ g/cm$^3)$, which decreases to about 0.94×10^{15} g/cm^3 with increasing Γ_{th}. Indeed, this is simply the consequence of the fact that increasing the thermal support against gravity leads to a less dense remnant. Interestingly, the temperature-dependent EOS leads to a remnant with an even smaller maximum rest-mass density $(\rho_{\text{max}} \approx 0.88 \times 10^{15}$ g/cm$^3)$ than the hybrid-EOS cases. This feature points to a systematic difference between the two types of simulations: While the hybrid method is by construction based on an EOS of cold betastable matter with thermal corrections, the full simulation produces matter strongly out of beta equilibrium, see the lowest panel of Fig. 4, as will be analyzed later.

On the other hand, the simulations carried out with the SFHo EOS show that the remnant collapses into a black hole after a time which strongly depends on the chosen thermodynamical treatment. In particular, the collapse takes place at $t \approx 13$ ms for the FT EOS and at $t \approx 7$ ms or $t \approx 14$ ms for the cases in which $\Gamma_{\text{th}} = 1.50$ or $\Gamma_{\text{th}} = 1.75$, respectively. Furthermore, before collapse, the fluctuations of the rest-mass density and temperature are more violent than for the V18 EOS during this metastable phase. While we focus here on the dependence of the collapse time on the temperature treatment, it has also been found to depend sizeably on the numerical resolution (see, e.g. Refs. [41,52]), which we have not been able to study here due to lack of numerical resources.
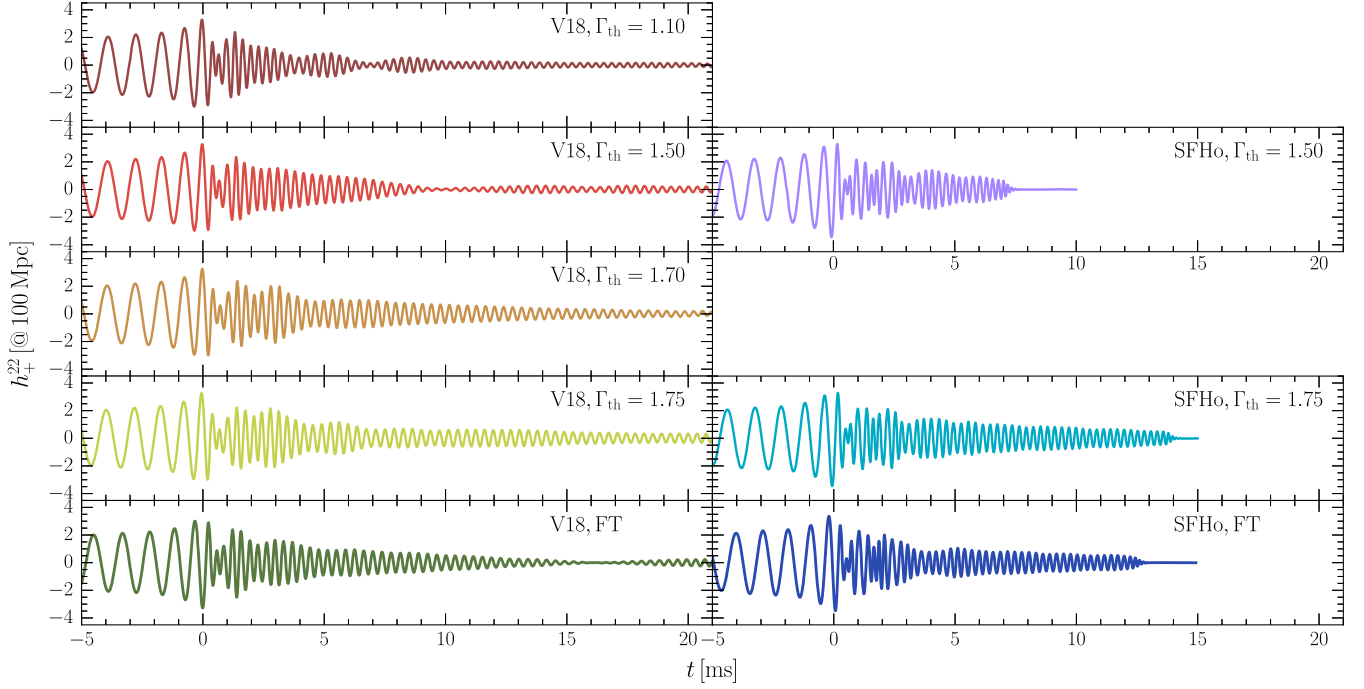
FIG. 5. Gravitational waveforms over a timescale of about 20 ms after the merger for the V18 and SFHo EOSs obtained for gravitational masses $2 \times 1.35 \, M_\odot$, comparing different choices of constant $\Gamma_{th} = 1.1, 1.5, 1.7, 1.75$ and the FT EOSs.

As mentioned previously, in addition to the maximum temperature for the FT simulations, whose values during the postmerger phase peak at around 70 and 110 MeV for the V18 and SFHo EOS respectively, we also report the density-weighted-average temperature. Note that for both EOSs, even during the inspiral, the average temperature is much smaller than the maximum values, which, especially during the inspiral, are reached only in small zones of the computational domain, as will be illustrated in Fig. 8.

We also confirm that, while during the inspiral phase there is no great deviation from betastability, with average values mostly below 5%, the postmerger remnant manifests important differences with respect to the latter, with average deviations of about 40% and 50% for V18 and SFHo respectively.

B. Gravitational-wave emission

In Fig. 5 we show the plus polarization of the $\ell = m = 2$ component of the gravitational-wave strains, which we label as h_+^{22}, for all the considered simulations we have carried out using the V18 and SFHo EOSs. As expected, no significant differences are found in the inspiral part of the signal; the only notable feature being that the time of merger, which we consider as the time corresponding to the maximum of the strain amplitude, varies slightly when varying Γ_{th} in the hybrid-EOS approach (the maximum variations are about 0.05 ms with respect to the average times calculated for both EOSs in the hybrid-EOS approach). The time of merger measured in the FT runs

for both the V18 and the SFHo EOS differs instead of ≈ 0.6 ms with respect to the average time calculated in the hybrid-EOS approach; we believe the small difference arises from the fact that while in the hybrid-EOS approach finite-temperature effects during the inspiral are minimized, the FT approach leads, especially in the final parts of the inspiral, to a temperature increase which, together with the slight deviation of betastability, could be responsible for this feature. On the other hand, as clearly shown in Fig. 5, we find that all the cases considered here exhibit very different postmerger profiles.

Figure 6 shows the power spectral density (PSD) plots of all simulations determined as detailed in the Appendix. In particular, we choose to study the dominant $\ell = m = 2$ mode, and consider the position of the f_2 peak (following the same nomenclature as in Ref. [56]) as a tracker of the different behaviors. Since especially for the V18-EOS case with higher Γ_{th} it is difficult to distinguish the dominant f_2 peaks, a fitting procedure represents the only way for an accurate determination of the f_2 positions (see the Appendix for a discussion on the determination of the values of the peaks). We report in Table II these values, together with their indetermination, the f_{max} values for each simulation, and the emitted gravitational-wave energy E_{GW} for the $\ell = m = 2$ mode, measured as outlined in the Appendix. In general, f_2 decreases and E_{GW} increases with increasing Γ_{th}, while the values of f_{max} depend only very weakly on Γ_{th} and do not show any specific dependence. As a result, and accounting for the fact that the determination of the f_2 peak frequency inevitably comes with a
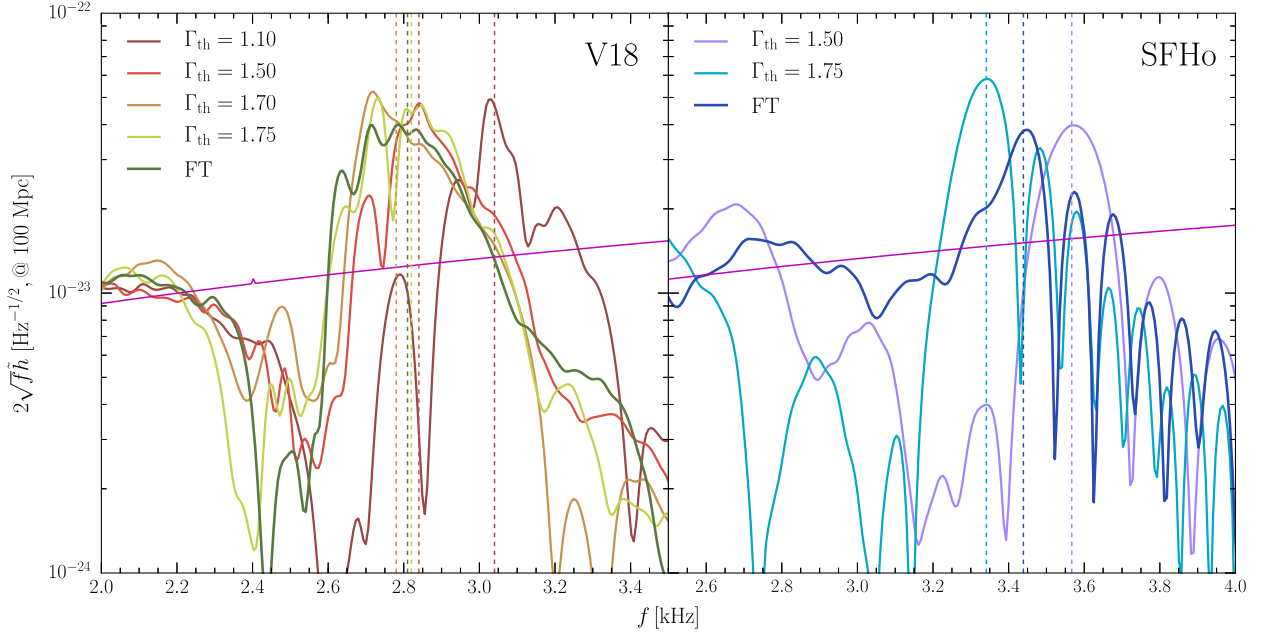
FIG. 6. PSDs of the simulations with the V18 and SFHo EOSs, at a distance of 100 Mpc. Vertical dashed lines of different colors indicate the frequency f_2. The sensitivity curve (magenta color) of Advanced LIGO is displayed for reference.

considerable uncertainty related to the different distributions of power in the various PSDs, the only robust conclusion that can be drawn from the data in Table II is that values of the thermal adiabatic index such that $\Gamma_{th} < 1.5$ are not in agreement with the results of the FT simulations. In the following sections we will seek other and more robust indicators of the optimal value for Γ_{th}.

We further note that the values of the f_2 frequencies reported in Table II agree reasonably well with both the universal relation between f_2 and the tidal polarizability parameter k_2^T [56] and the radius of a 1.6 $M_\odot$ NS, $R_{1.6}$ [88], which we report for completeness:

$$f_2 \approx 5.832 - 1.118(k_2^T)^{1/5} \approx 2.95 \text{ [kHz]}, \qquad (17)$$

$$f_2 \approx 8.713 - 0.4667 R_{1.6} \approx 2.86 \text{ [kHz]}, \qquad (18)$$

TABLE II. GW properties of NSs for the considered EOSs: instantaneous frequency at amplitude maximum f_{max}, frequency of the f_2 peak, and the total emitted energy E_{GW}.

Simulation	f_{max} (kHz)	f_2 (kHz)	E_{GW} (10^{52} erg)
V18—FT	1.77	2.81 ± 0.02	5.28
V18—$\Gamma_{th} = 1.75$	1.79	2.82 ± 0.08	5.84
V18—$\Gamma_{th} = 1.7$	1.77	2.78 ± 0.07	5.68
V18—$\Gamma_{th} = 1.5$	1.79	2.84 ± 0.01	4.97
V18—$\Gamma_{th} = 1.1$	1.81	3.04 ± 0.01	4.46
SFHo—FT	1.95	3.44 ± 0.01	6.89
SFHo—$\Gamma_{th} = 1.75$	1.92	3.34 ± 0.01	7.80
SFHo—$\Gamma_{th} = 1.5$	1.93	3.57 ± 0.01	6.38

where $k_2^T = 113.08$, $R_{1.6} = 12.54$ km for the V18 EOS, while $k_2^T = 78.75$, $R_{1.6} = 11.77$ km for the SFHo EOS.

We also find that the simulation employing the V18 EOS with $\Gamma_{th} = 1.1$ yields the highest frequency of the f_2 peak ($\sim$230 Hz above the FT value). Such a finding is in agreement with the behavior of the rest-mass density found in Fig. 4. In particular, since the frequency of the mode scales with the square root of the average density (see, e.g., Ref. [89]), the behavior of the f_2 peak confirms spectroscopically that in this case the remnant not only has the largest central density, but it also has the largest average rest-mass density and is therefore subject to the fastest oscillations among all the cases considered.

C. Differential rotation and effective thermal adiabatic index

In the following we analyze in more detail the properties of the remnant that is formed after merger. Figure 7, in particular, shows the one-dimensional radial profiles of the averaged rest-mass density (left panel) and of the angular velocity (right panel) for all the cases we have considered at a time $t \approx 14$ ms after the merger. The profiles are obtained from the values of the corresponding quantity on the equatorial plane ($z = 0$) and after averaging in the azimuthal direction and over a time window of 1 ms so as to obtain functions that depend only on the cylindrical radius, r, from the center of the grid.

In the bottom part of each panel we also report the fractional differences of the hybrid-EOS profiles with respect to the fiducial FT ones. Overall, we find that in the core of the remnant (i.e., $r \lesssim 6$ km), differences in
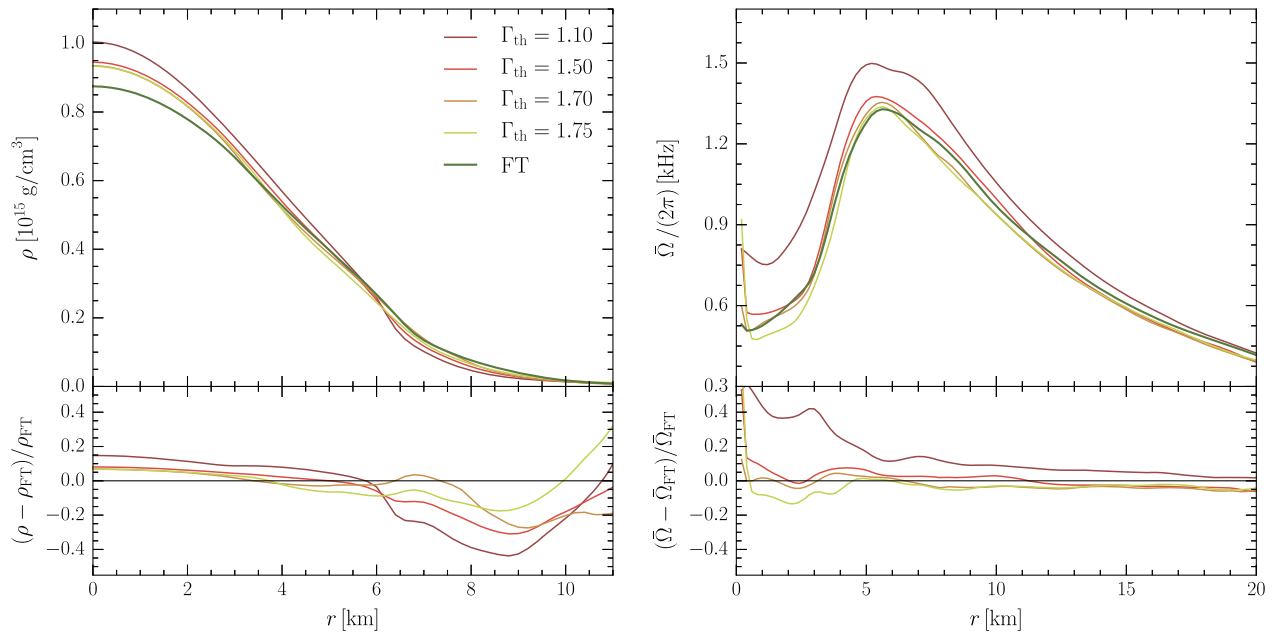
FIG. 7. Average rest-mass density and angular velocity for the different V18-based EOSs as a function of the radial coordinate r ($z = 0$) at $t = 14$ ms.

density remain below 10% for the cases $\Gamma_{\text{th}} = 1.5$, 1.7, 1.75, while they increase below $\rho \approx 2 \times 10^{14}$ g/cm^3. Interestingly, the case $\Gamma_{\text{th}} = 1.1$ always shows the largest differences and the case $\Gamma_{\text{th}} = 1.7$ the smallest fractional differences in the core area, which is dynamically the most important one.

In order to determine which values of Γ_{th} best approximate the FT behavior, we compute such values pointwise according to Eq. (12), using the local values of ρ, x_p, and T obtained in the FT simulations and the FT tables to compute p and ε. Note, however, that while Γ_{th} is used in simulations where the betastability is enforced throughout the evolution, this way of computing Γ_{th} ignores the

betastability condition of cold matter, since x_p—which is evaluated pointwise in the FT simulations—is not the proton fraction of cold betastable matter. The method is most close to the fixed-x_p prescription used in Fig. 1 with $x_p(T > 0)$, but the FT x_p is not the one of hot betastable matter either. As a result, it can only give an approximate indication of the "best" value to be used in hybrid-EOS calculations (see also the previous discussion in Sec. II D).

Figure 8 shows in the top-left quadrants the values of the "local" Γ_{th} on the $z = 0$ plane at time $t = 9$ ms after the merger. Other quantities reported are the distributions of the rest-mass density ρ (top-right quadrants), the temperature T (bottom-right quadrants), and the deviation of the electron
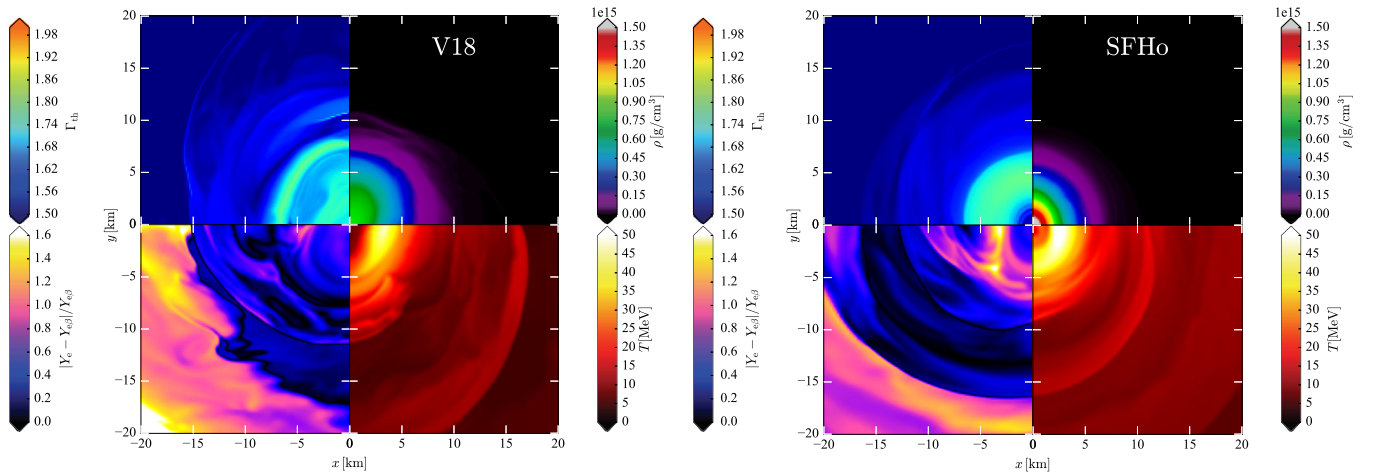

FIG. 8. Distributions of Γ_{th}, Eq. (12), (upper-left side of the figures), rest-mass density (upper right), temperature (lower right), and deviation from betastability (lower left), in the $z = 0$ plane at $t \approx 9$ ms after the merger.

fraction from its betastable value, $|Y_{e\beta} - Y_e|/Y_{e\beta}$ (bottom-left quadrants). Note that while in the hybrid-EOS simulations Γ_{th} is, by construction, constant over the computational domain, in the FT case the computed value with the V18 EOS (right panel) is generally $\Gamma_{th} \lesssim 1.6$ for $\rho \lesssim 5 \times 10^{13}$ g/cm^3, and very close to $\Gamma_{th} \simeq 1.7$ for higher densities and hence in the core of the HMNS.

On the other hand, the SFHo simulation (right panel) exhibits a slightly different behavior, with $\Gamma_{th} \gtrsim 1.7$ in the density region $10^{14} \lesssim \rho/\text{g/cm}^3 \lesssim 10^{15}$ and with the highest-density region being instead dominated by values $\Gamma_{th} \lesssim 1.65$. This behavior confirms qualitatively the conclusions drawn from Fig. 6, namely, that a value of the thermal adiabatic index $\Gamma_{th} \approx 1.7$ provides a good match to the postmerger spectroscopic properties observed in the two FT EOSs.

The temperature distributions reported in Fig. 8 show the typical appearance of two hot spots of more than 50 MeV [44,90], whose temperature evolution was shown in Fig. 4 and whose appearance can be associated with the conservation of the Bernoulli constant (see [44] for a detailed discussion). The two hot spots eventually merge into an axisymmetric structure after $t \simeq 22$ ms. Also quite evident from the bottom-left quadrants is that the matter after the merger is significantly out of beta equilibrium, especially in the low-density layers of the HMNS. Averaged values were plotted in Fig. 4. As discussed above, this deviation limits the validity of the comparison of the dynamical and thermodynamical properties of the matter between simulations carried out with the FT EOSs and with hybrid EOSs.

It is also clearly visible from the top-left quadrants in Fig. 8 that the local value Γ_{th} is far from being constant, but depends strongly on the density, temperature, and proton (electron) fraction at each point of the computational domain. Notwithstanding these limitations, we can nevertheless attempt to identify in FT simulations a reference value of Γ_{th} by considering a spatial average and by inspecting how much this average varies with time. For this purpose we calculate, on the equatorial plane ($z = 0$) and at each time t after the merger, the density-weighted spatial average of Γ_{th} as [cf. Eq. (15) for the density-weighted-average temperature]

$$\langle \Gamma_{th} \rangle \equiv \frac{\int dV \rho \Gamma_{th}}{\int dV \rho}, \qquad (19)$$

where, again, the average is performed after applying a low-density threshold of 10^{13} g/cm^3 to avoid contamination from the dynamically unimportant matter. We have verified that the results are insensitive to changes of this threshold, with deviations of Γ_{th} of the order 3×10^{-3} when 10^{12} g/cm^3 is chosen instead.

Figure 9 reports the evolution of the average thermal adiabatic index, in a time window between 5 and 10 ms after merger, which corresponds to the time interval when
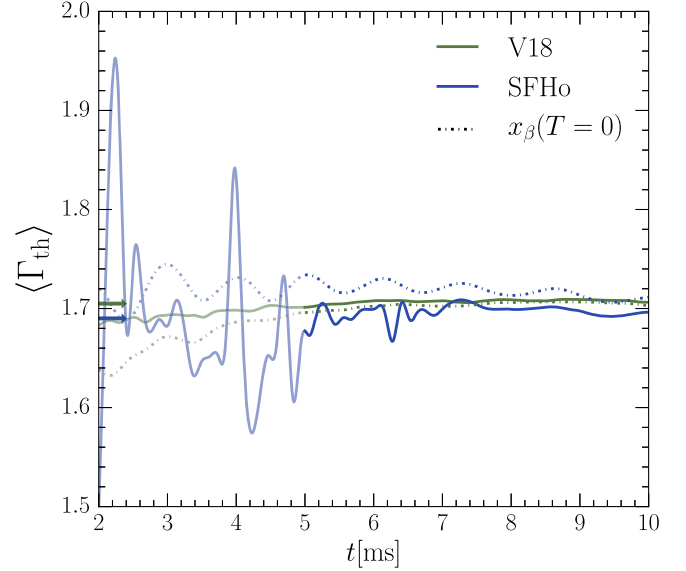

FIG. 9. The average Γ_{th}, Eq. (19), as a function of time for the FT V18 and SFHo simulations. Time averages related to the total time interval considered here are represented as arrows in the plot. Dot-dashed curves represent the average values of Γ_{th} calculated using Eq. (12) with $x_p = x_\beta(\rho, T = 0)$, as described in the text.

the fluctuations of Γ_{th} for the SFHo EOS are minimal and a comparison between FT and hybrid EOSs is more reasonable. We notice that, for both EOSs, $\langle \Gamma_{th} \rangle \simeq 1.7$, and that the corresponding time and spatial averages for the V18 and the SFHo EOS are $\langle \bar{\Gamma}_{th} \rangle = 1.705$ and $\langle \bar{\Gamma}_{th} \rangle = 1.690$, respectively (indicated by arrows). These averages include also the initial time interval, $2 \lesssim t/\text{ms} \lesssim 5$, when the HMNS has just been formed and the dynamics is still very far from being quasistationary (light-colored curve segments). As a further confirmation of our results, we also report the average of Γ_{th} calculated using the values of p and e evaluated employing x_β at $T = 0$ (instead of the local value of x_p, as we have done in Fig. 2 (dash-dotted curves). We find also in this case good agreement with the value 1.7 for both EOSs.

Figure 10 shows a selection of Γ_{th} isocontours on the $z = 0$ plane for the time window between 5 and 10 ms also considered for Fig. 9. We find that the distribution shown in Fig. 8 remains robust for the time window considered; in particular, for both V18 and SFHo the Γ_{th} distribution peaks off-center. We notice that V18 is characterized by two stable and narrow peak structures at about 3 and 7 km, while SFHo shows a broader peak region, approximately comprised between 3 and 6 km. The high-density regions also show important differences being characterized by higher Γ_{th} for V18 and values even lower than 1.5 for SFHo. The latter case shows local strong oscillations about the center which are evident for the first ms of the time window we show, representing a residual of the stronger oscillations affecting the previous part of the simulation.
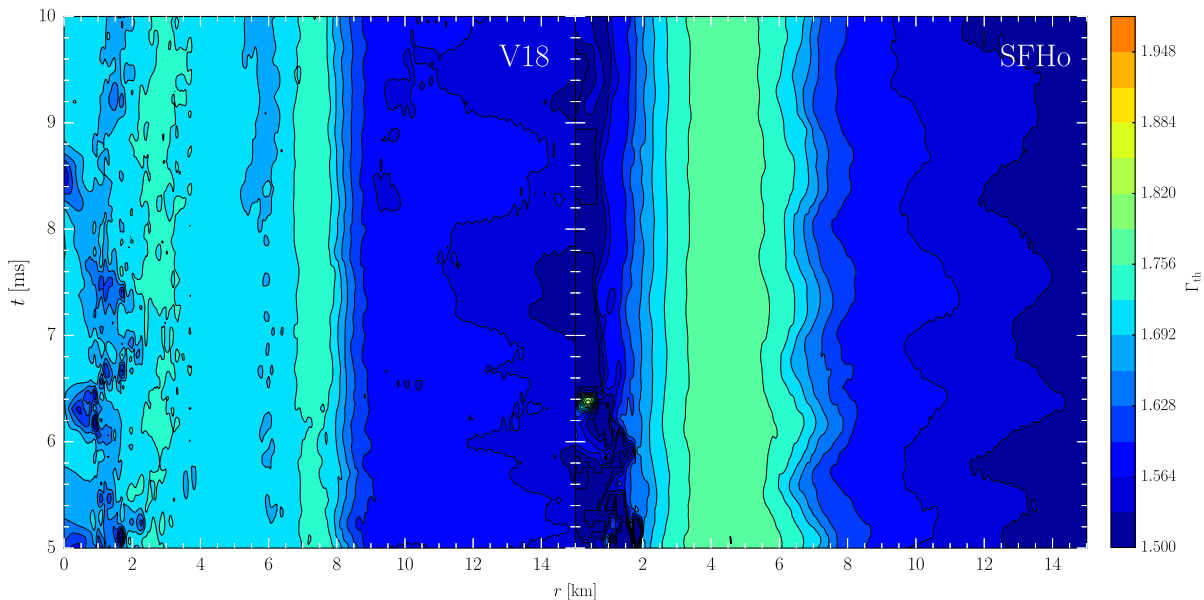
FIG. 10.   Isocontours of Γ_{th} as a function of cylindrical radius r and time t for the V18 and SFHo FT simulations.

In summary, on the basis of the various measurements and diagnostics discussed so far, we conclude that using a hybrid EOS to simulate the merger of binary NS systems, the value of thermal adiabatic index $\Gamma_{th} \approx 1.7$ best approximates the dynamical and thermodynamical behavior of matter computed using complete, finite-temperature EOSs.

V. CONCLUSIONS

Hybrid EOSs, in which thermal contributions are artificially added in terms of an ideal-fluid EOS, are widely adopted in the numerical modeling of merging binary NSs. This is in part due to the smaller computational costs that are associated with hybrid EOSs, but, more importantly, it is the consequence of the scarcity of full temperature-dependent EOSs that can be employed in numerical simulations. The use of such hybrid EOSs, however, also raises the fundamental problem of deciding which value should be given and kept constant—both in space and time—to the thermal adiabatic index Γ_{th}, which is instead expected to change both in space and time.

In order to address this point, and hence determine the optimal value for Γ_{th}, we have carried out a number of simulations of merging neutron stars in full general relativity, employing two fully tabulated, temperature-dependent EOSs and a neutrino-leakage scheme for the treatment of neutrinos. The first of these temperature-dependent EOSs, the V18 EOS, has been derived in the BHF formalism that fulfills all the current constraints imposed by the nuclear phenomenology, and also respects recent observational limits on the maximum NS mass and deformability; the V18 EOS has been employed here for the first time in merger simulations. The second temperature-dependent EOS, the SFHo EOS, is based on a RMF model which takes into account a statistical ensemble of nuclei and interacting nucleons; the SFHo EOS has been employed routinely in the past to model merging NS binaries.

Together with the temperature-dependent EOSs, we have also performed similar simulations employing hybrid EOSs where we have considered a variety of values for the thermal adiabatic index Γ_{th} and where the cold part is given by the slice at $T = 0$ of the temperature-dependent EOSs. In this way, we have been able to construct instances of the binaries that were virtually the same during the inspiral—when thermal effects are dynamically unimportant—and that start to differ from the merger, as the thermal contributions from the two classes of EOSs are important and different.

We have then used and monitored a number of different quantities relative either to the matter sector—e.g., rest-mass density, temperature, electron fraction, angular velocity of the merged object—or to the gravitational-field sector—e.g., gravitational waves and PSDs of the post-merger signal. Furthermore, we have performed measurements of the effective thermal adiabatic index and followed its distribution in space and its evolution in time. The importance of ambiguities in its definition due to the loss of beta equilibrium during the postmerger simulation have been evidenced. In this way, and collecting the information from all of these quantities, we have concluded that a value of $\Gamma_{th} \approx 1.7$ best approximates the complete, finite-temperature EOS in binary NS simulations. This value is similar to the standard one employed in numerical simulations so far (i.e., $\Gamma_{th} = 1.75$–1.80), but also importantly lower. Future work will be aimed at increasing the robustness of this finding by employing other temperature-dependent EOSs, including those presented recently in Ref. [7].

APPENDIX A: GRAVITATIONAL-WAVE SIGNAL

We extract the gravitational-wave signal using the standard Newman-Penrose formalism [91]: We calculate the Newman-Penrose scalar ψ_4 at different surfaces of constant coordinate radius r using the Einstein Toolkit module WeylScal4. In particular, ψ_4 is related to the second time derivatives of the gravitational-wave polarization amplitudes h_+ and $h_\times$ by

$$\psi_4 = \ddot{h}_+ - i\ddot{h}_\times = \sum_{l=2}^{\infty} \sum_{m=-l}^{l} \psi_4^{\ell m}(t,r) {}_{-2}Y_{\ell m}(\theta,\phi), \quad (A1)$$

where the double dot represents the second time derivative and we have introduced also the MULTIPOLE expansion of ψ_4 in spin-weighted spherical harmonics [92] of spin weight $s = -2$ (such decomposition is performed by the module MULTIPOLE). As the dominant mode is $\ell = m = 2$, we restrict our analysis only to the latter; i.e., we assume

$$h_{+,\times} = \sum_{l=2}^{\infty} \sum_{m=-l}^{l} h_{+,\times}^{\ell m}(t,r) {}_{-2}Y_{\ell m}(\theta,\phi) \approx h_{+,\times}^{22} {}_{-2}Y_{22}(\theta,\phi). \quad (A2)$$

The fixed-frequency integration described in [93] is carried out in order to double integrate ψ_4 in time. We then align our waveforms, as in [56], to the "time of the merger", which we set as $t = 0$ and we define as the time when the GW amplitude

$$|h| \equiv \sqrt{h_+^2 + h_\times^2} \quad (A3)$$

is maximal. We also compute the phase of the complex waveform, which we label with $\chi = \arctan(h_\times/h_+)$, and

the instantaneous frequency of the gravitational waves defined as in [94],

$$f_{GW} \equiv \frac{1}{2\pi}\frac{d\chi}{dt}. \quad (A4)$$

We identify, as in [56], $f_{max} \equiv f_{GW}(t = 0)$ as the instantaneous frequency at amplitude maximum.

The total emitted energy for the $\ell = m = 2$ mode is

$$E_{GW} = \frac{R^2}{16\pi}\int dt \int d\Omega \, |\dot{h}(t,\theta,\phi)|^2, \quad (A5)$$

where Ω is the solid angle and R represents the source-detector distance.

We also consider the PSD of the effective amplitude defined as

$$\tilde{h}(f) \equiv \sqrt{\frac{|\tilde{h}_+(f)|^2 + |\tilde{h}_\times(f)|^2}{2}}, \quad (A6)$$

where $\tilde{h}_{+,\times}(f)$ are the Fourier transforms of $h_{+,\times}$,

$$\tilde{h}_{+,\times}(f) \equiv \int dt \, e^{-i2\pi ft} h_{+,\times}(t) \quad (A7)$$

for $f \geq 0$, and $\tilde{h}_{+,\times}(f) \equiv 0$ for $f < 0$. We determine the position of the f_2 peak of the PSD, after applying a symmetric time-domain Tukey filter with parameter $\alpha = 0.25$ to the waveforms, in order to compute PSDs without the artificial noise due to the truncation of the waveform. We then fit our data with the analytic function [55]

$$S_2(f) = A_{2G}e^{-(f-F_{2G})^2/W_{2G}^2} + A(f)\gamma(f), \quad (A8)$$

where

$$A(f) \equiv \frac{1}{2W_2}[(A_{2b} - A_{2a})(f - F_2) + W_2(A_{2b} + A_{2a})], \quad (A9)$$

$$\gamma(f) \equiv (1 + e^{-(f-F_2+W_2)/s})^{-1}(1 + e^{(f-F_2-W_2)/s})^{-1}. \quad (A10)$$

The peak frequency is then determined by

$$f_2 \equiv \frac{\int df S_2(f)f}{\int df S_2(f)}. \quad (A11)$$

This fitting procedure manifests an intrinsic uncertainty due to both the choice of the fitting functions and parameters, and the integration interval, which we estimate as ± 10 Hz. Such indetermination is later added in quadrature to a systematic deviation of the value we find for f_2

from the nearest (local) maximum of the PSD curve. The latter estimate coincides with the deviation with respect to the global maximum of the PSD for all the cases considered apart from the $\Gamma_{th} = 1.75$ case, where the presence of a second narrower peak located at lower frequencies determines a higher indetermination. The case $\Gamma_{th} = 1.7$ also shows the same feature, with the two peaks being indistinguishable with respect to each other. Table II reports the total indetermination for each case, namely, the sum in quadrature of the intrinsic uncertainty and the deviation with respect to the global maximum of the PSD curves.

---

[1] B. P. Abbott, R. Abbott, T. D. Abbott, F. Acernese, K. Ackley, C. Adams, T. Adams, P. Addesso, R. X. Adhikari, V. B. Adya *et al.* (LIGO Scientific and Virgo Collaborations), Phys. Rev. Lett. **119,** 161101 (2017).

[2] B. P. Abbott, R. Abbott, T. D. Abbott, F. Acernese, K. Ackley, C. Adams, T. Adams, P. Addesso, R. X. Adhikari, V. B. Adya *et al.* (LIGO Scientific and Virgo Collaborations), Phys. Rev. Lett. **121,** 161101 (2018).

[3] J.-B. Wei, J.-J. Lu, G. F. Burgio, Z. H. Li, and H. J. Schulze, Eur. Phys. J. A **56,** 63 (2020).

[4] G. F. Burgio, A. Drago, G. Pagliara, H.-J. Schulze, and J.-B. Wei, Astrophys. J. **860,** 139 (2018).

[5] J.-B. Wei, A. Figura, G. F. Burgio, H. Chen, and H.-J. Schulze, J. Phys. G **46,** 034001 (2019).

[6] A. Bauswein, H. T. Janka, and R. Oechslin, Phys. Rev. D **82,** 084043 (2010).

[7] J.-J. Lu, Z.-H. Li, G. F. Burgio, A. Figura, and H. J. Schulze, Phys. Rev. C **100,** 054335 (2019).

[8] M. Baldo, *Nuclear Methods and Nuclear Equation of State (International Review of Nuclear Physics)* (World Scientific Publishing Company, Inc, Singapore, 1999).

[9] O. E. Nicotra, M. Baldo, G. F. Burgio, and H. J. Schulze, Astron. Astrophys. **451,** 213 (2006).

[10] O. E. Nicotra, M. Baldo, G. F. Burgio, and H. J. Schulze, Phys. Rev. D **74,** 123001 (2006).

[11] A. Li, X. R. Zhou, G. F. Burgio, and H. J. Schulze, Phys. Rev. C **81,** 025806 (2010).

[12] G. F. Burgio, H. J. Schulze, and A. Li, Phys. Rev. C **83,** 025804 (2011).

[13] G. F. Burgio and H. J. Schulze, Astron. Astrophys. **518,** A17 (2010).

[14] C. Bloch and C. De Dominicis, Nucl. Phys. **7,** 459 (1958).

[15] A. Lejeune, P. Grangé, M. Martzolff, and J. Cugnon, Nucl. Phys. **A453,** 189 (1986).

[16] M. Baldo and L. S. Ferreira, Phys. Rev. C **59,** 682 (1999).

[17] R. B. Wiringa, V. G. J. Stoks, and R. Schiavilla, Phys. Rev. C **51,** 38 (1995).

[18] W. Zuo, A. Lejeune, U. Lombardo, and J. F. Mathiot, Nucl. Phys. **A706,** 418 (2002).

[19] Z.-H. Li, U. Lombardo, H. J. Schulze, and W. Zuo, Phys. Rev. C **77,** 034316 (2008).

[20] Z.-H. Li and H. J. Schulze, Phys. Rev. C **78,** 028801 (2008).

[21] P. Grangé, A. Lejeune, M. Martzolff, and J.-F. Mathiot, Phys. Rev. C **40,** 1040 (1989).

[22] W. Zuo, Z. H. Li, A. Li, and G. C. Lu, Phys. Rev. C **69,** 064001 (2004).

[23] I. Bombaci and U. Lombardo, Phys. Rev. C **44,** 1892 (1991).

[24] W. Zuo, I. Bombaci, and U. Lombardo, Phys. Rev. C **60,** 024605 (1999).

[25] G. Taranto, M. Baldo, and G. F. Burgio, Phys. Rev. C **87,** 045803 (2013).

[26] H. Shen, H. Toki, K. Oyamatsu, and K. Sumiyoshi, Astrophys. J. Suppl. Ser. **197,** 20 (2011).

[27] D. Radice, L. Rezzolla, and F. Galeazzi, Classical Quantum Gravity **31,** 075012 (2014).

[28] M. Hempel and J. Schaffner-Bielich, Nucl. Phys. **A837,** 210 (2010).

[29] M. Hempel, T. Fischer, J. Schaffner-Bielich, and M. Liebendörfer, Astrophys. J. **748,** 70 (2012).

[30] J. M. Lattimer and F. D. Swesty, Nucl. Phys. **A535,** 331 (1991).

[31] H. Shen, H. Toki, K. Oyamatsu, and K. Sumiyoshi, Nucl. Phys. **A637,** 435 (1998).

[32] Y. Sugahara and H. Toki, Nucl. Phys. **A579,** 557 (1994).

[33] A. W. Steiner, M. Hempel, and T. Fischer, Astrophys. J. **774,** 17 (2013).

[34] G. Colò, N. V. Giai, J. Meyer, K. Bennaceur, and P. Bonche, Phys. Rev. C **70,** 024307 (2004).

[35] G. Fiorella Burgio and A. F. Fantina, in *The Physics and Astrophysics of Neutron Stars*, Astrophysics and Space Science Library Vol. 457, edited by L. Rezzolla, P. Pizzochero, D. I. Jones, N. Rea, and I. Vidaña (Springer, Cham, 2018), p. 255.

[36] H. T. Cromartie *et al.*, Nat. Astron. **4,** 72 (2020).

[37] A. Carbone, Phys. Rev. Research **2,** 023227 (2020).

[38] H.-T. Janka, T. Zwerger, and R. Mönchmeyer, Astron. Astrophys. **268,** 360 (1993).

[39] L. Baiotti, B. Giacomazzo, and L. Rezzolla, Phys. Rev. D **78,** 084033 (2008).

[40] K. Hotokezaka, K. Kyutoku, H. Okawa, M. Shibata, and K. Kiuchi, Phys. Rev. D **83,** 124008 (2011).

[41] K. Kiuchi, K. Kyutoku, Y. Sekiguchi, M. Shibata, and T. Wada, Phys. Rev. D **90,** 041502(R) (2014).

[42] R. De Pietri, A. Feo, F. Maione, and F. Löffler, Phys. Rev. D **93,** 064047 (2016).

[43] A. Endrizzi, R. Ciolfi, B. Giacomazzo, W. Kastaun, and T. Kawamura, Classical Quantum Gravity **33,** 164001 (2016).

[44] M. Hanauske, K. Takami, L. Bovard, L. Rezzolla, J. A. Font, F. Galeazzi, and H. Stöcker, Phys. Rev. D **96,** 043004 (2017).

[45] R. Ciolfi, W. Kastaun, B. Giacomazzo, A. Endrizzi, D. M. Siegel, and R. Perna, Phys. Rev. D **95**, 063016 (2017).

[46] M. Shibata and K. Kiuchi, Phys. Rev. D **95**, 123003 (2017).

[47] D. Radice, A. Perego, S. Bernuzzi, and B. Zhang, Mon. Not. R. Astron. Soc. **481**, 3670 (2018).

[48] D. Radice, A. Perego, K. Hotokezaka, S. A. Fromm, S. Bernuzzi, and L. F. Roberts, Astrophys. J. **869**, 130 (2018).

[49] M. G. Alford, L. Bovard, M. Hanauske, L. Rezzolla, and K. Schwenzer, Phys. Rev. Lett. **120**, 041101 (2018).

[50] A. Endrizzi, D. Logoteta, B. Giacomazzo, I. Bombaci, W. Kastaun, and R. Ciolfi, Phys. Rev. D **98**, 043015 (2018).

[51] K. Kiuchi, K. Kyutoku, M. Shibata, and K. Taniguchi, Astrophys. J. **876**, L31 (2019).

[52] R. De Pietri, A. Feo, J. A. Font, F. Löffler, M. Pasquali, and N. Stergioulas, Phys. Rev. D **101**, 064052 (2020).

[53] L. Rezzolla and O. Zanotti, *Relativistic Hydrodynamics* (Oxford University Press, Oxford, 2013).

[54] K. Takami, L. Rezzolla, and L. Baiotti, Phys. Rev. Lett. **113**, 091104 (2014).

[55] K. Takami, L. Rezzolla, and L. Baiotti, Phys. Rev. D **91**, 064001 (2015).

[56] L. Rezzolla and K. Takami, Phys. Rev. D **93**, 124051 (2016).

[57] S. Banik, M. Hempel, and D. Bandyopadhyay, Astrohys. J. Suppl. Ser. **214**, 22 (2014).

[58] S. Typel, G. Röpke, T. Klähn, D. Blaschke, and H. H. Wolter, Phys. Rev. C **81**, 015803 (2010).

[59] H. Togashi, E. Hiyama, Y. Yamamoto, and M. Takano, Phys. Rev. C **93**, 035808 (2016).

[60] E. R. Most, L. Jens Papenfort, V. Dexheimer, M. Hanauske, H. Stoecker, and L. Rezzolla, Eur. Phys. J. A **56**, 59 (2020).

[61] J. Antoniadis, P. C. C. Freire, N. Wex, T. M. Tauris, R. S. Lynch *et al.*, Science **340**, 1233232 (2013).

[62] S. Koeppel, L. Bovard, and L. Rezzolla, Astrophys. J. Lett. **872**, L16 (2019).

[63] L. J. Papenfort, R. Gold, and L. Rezzolla, Phys. Rev. D **98**, 104028 (2018).

[64] LORENE, Langage Objet pour la RElativité Numérique, http://www.lorene.obspm.fr.

[65] E. Gourgoulhon, P. Grandclément, K. Taniguchi, J. A. Marck, and S. Bonazzola, Phys. Rev. D **63**, 064029 (2001).

[66] A. Carbone and A. Schwenk, Phys. Rev. C **100**, 025805 (2019).

[67] D. Brown, P. Diener, O. Sarbach, E. Schnetter, and M. Tiglio, Phys. Rev. D **79**, 044023 (2009).

[68] F. Loeffler, J. Faber, E. Bentivegna, T. Bode, P. Diener, R. Haas, I. Hinder, B. C. Mundim, C. D. Ott, E. Schnetter, G. Allen, M. Campanelli, and P. Laguna, Classical Quantum Gravity **29**, 115001 (2012).

[69] D. Alic, C. Bona-Casas, C. Bona, L. Rezzolla, and C. Palenzuela, Phys. Rev. D **85**, 064040 (2012).

[70] D. Alic, W. Kastaun, and L. Rezzolla, Phys. Rev. D **88**, 064049 (2013).

[71] M. Bezares, C. Palenzuela, and C. Bona, Phys. Rev. D **95**, 124005 (2017).

[72] M. Alcubierre, B. Brügmann, P. Diener, M. Koppitz, D. Pollney, E. Seidel, and R. Takahashi, Phys. Rev. D **67**, 084023 (2003).

[73] D. Pollney *et al.*, Phys. Rev. D **76**, 124002 (2007).

[74] D. Radice, L. Rezzolla, and F. Galeazzi, Mon. Not. R. Astron. Soc. Lett. **437**, L46 (2014).

[75] D. Radice, L. Rezzolla, and F. Galeazzi, ASP Conf. Ser. **498**, 121 (2015).

[76] A. Suresh and H. T. Huynh, J. Comput. Phys. **136**, 83 (1997).

[77] D. Radice and L. Rezzolla, Astron. Astrophys. **547**, A26 (2012).

[78] D. Radice, L. Rezzolla, and T. Kellerman, Classical Quantum Gravity **27**, 235015 (2010).

[79] F. Galeazzi, W. Kastaun, L. Rezzolla, and J. A. Font, Phys. Rev. D **88**, 064009 (2013).

[80] D. Radice, F. Galeazzi, J. Lippuner, L. F. Roberts, C. D. Ott, and L. Rezzolla, Mon. Not. R. Astron. Soc. **460**, 3255 (2016).

[81] H. O. Kreiss and J. Oliger, *Methods for the Approximate Solution of Time Dependent Problems*, GARP Publication Series No. 10 (Global Atmospheric Research Programme - WMO-ICSU Joint Organizing Committee, Geneva, 1973).

[82] E. Schnetter, S. H. Hawley, and I. Hawke, Classical Quantum Gravity **21**, 1465 (2004).

[83] https://github.com/bhfeos/FTEOS.

[84] R. Gill, A. Nathanail, and L. Rezzolla, Astrophys. J. **876**, 139 (2019).

[85] E. R. Most, L. J. Papenfort, V. Dexheimer, M. Hanauske, S. Schramm, H. Stöcker, and L. Rezzolla, Phys. Rev. Lett. **122**, 061101 (2019).

[86] E. R. Most, L. J. Papenfort, and L. Rezzolla, Mon. Not. R. Astron. Soc. **490**, 3588 (2019).

[87] A. Perego, S. Bernuzzi, and D. Radice, Eur. Phys. J. A **55**, 124 (2019).

[88] A. Bauswein, H.-T. Janka, K. Hebeler, and A. Schwenk, Phys. Rev. D **86**, 063001 (2012).

[89] K. D. Kokkotas and B. G. Schmidt, Living Rev. Relativity **2**, 2 (1999).

[90] W. Kastaun and F. Galeazzi, Phys. Rev. D **91**, 064027 (2015).

[91] E. T. Newman and R. Penrose, J. Math. Phys. (N.Y.) **3**, 566 (1962); **4**, 998(E) (1963).

[92] J. N. Goldberg, A. J. MacFarlane, E. T. Newman, F. Rohrlich, and E. C. G. Sudarshan, J. Math. Phys. (N.Y.) **8**, 2155 (1967).

[93] C. Reisswig and D. Pollney, Classical Quantum Gravity **28**, 195015 (2011).

[94] J. S. Read, L. Baiotti, J. D. E. Creighton, J. L. Friedman, B. Giacomazzo, K. Kyutoku, C. Markakis, L. Rezzolla, M. Shibata, and K. Taniguchi, Phys. Rev. D **88**, 044042 (2013).